

Interfacial Thermal Conductance of Thiolate-Protected Gold Nanospheres

Kelsey M. Stocker, Suzanne M. Neidhart, and J. Daniel Gezelter^{a)}

*Department of Chemistry and Biochemistry, University of Notre Dame, Notre Dame,
IN 46556*

Molecular dynamics simulations of thiolate-protected and solvated gold nanoparticles were carried out in the presence of a non-equilibrium heat flux between the solvent and the core of the particle. The interfacial thermal conductance (G) was computed for these interfaces, and the behavior of the thermal conductance was studied as a function of particle size, ligand flexibility, and ligand chain length. In all cases, thermal conductance of the ligand-protected particles was higher than the bare metal–solvent interface. A number of mechanisms for the enhanced conductance were investigated, including thiolate-driven corrugation of the metal surface, solvent ordering at the interface, solvent-ligand interpenetration, and ligand ordering relative to the particle surface. Only the smallest particles exhibited significant corrugation. All ligands permitted substantial solvent-ligand interpenetration, and ligand chain length has a significant influence on the orientational ordering of interfacial solvent. Solvent – ligand vibrational overlap, particularly in the low frequency range ($< 80\text{cm}^{-1}$) was significantly altered by ligand rigidity, and had direct influence on the interfacial thermal conductance.

^{a)}Electronic mail: gezelter@nd.edu

I. INTRODUCTION

Heat transport across various nanostructured interfaces has been the subject of intense experimental interest,¹⁻⁸ and the interfacial thermal conductance, G , is the principal quantity of interest for understanding interfacial heat transport.⁹ Because nanoparticles have a significant fraction of their atoms at the particle / solvent interface, the chemical details of these interfaces govern the thermal transport properties. Time-domain thermoreflectance (TDTR) measurements on planar self-assembled monolayer (SAM) junctions between quartz and gold films showed that surface chemistry, particularly the density of covalent bonds to the gold surface, can control energy transport between the two solids.¹⁰ Experiments and simulations on three-dimensional nanocrystal arrays have similarly shown that surface-attached ligands mediate the thermal transport in these materials, placing particular importance on the overlap between the ligand and nanoparticle vibrational densities of states.^{11,12} Likewise, simulations of polymer-coated gold nanoparticles in water have shown that the surface coating introduces a dominant thermal transport channel to the surrounding solvent.¹³

For ligand-protected nanoparticles in a solvent, there may be three distinct heat transfer processes: (1) from the particles to the ligands, (2) vibrational energy transfer along the length of the ligand, followed by (3) heat transport from the ligand to the surrounding solvent.¹⁴

Heat transport at the gold-alkylthiolate-solvent interface has been previously explored both through molecular dynamics simulations and via TDTR.¹⁵⁻¹⁸ Most of these studies have found that alkylthiolates enhance the thermal conductance to the solvent, and that the vibrational overlap provided by the chemically-bound ligand species plays a role in this enhancement.

Reverse nonequilibrium molecular dynamics (RNEMD) methods¹⁹ have been previously applied to calculate the thermal conductance at flat (111) metal / organic solvent interfaces that had been chemically protected by varying coverages of alkanethiolate groups.¹⁶ These simulations suggested an explanation for the increased thermal conductivity at alkanethiol-capped metal surfaces compared with bare metal interfaces. Specifically, the chemical bond between the metal and the ligand introduces a vibrational overlap that is not present without the protecting group, and the overlap between the vibrational spectra (metal to ligand, ligand to solvent) provides a mechanism for rapid thermal transport across the interface. The simulations also suggested that this phenomenon is a non-monotonic function of the fractional coverage of the surface, as moderate coverages allow energy transfer to solvent molecules that come into close contact with the ligands.

Similarly, simulations of *mixed-chain* alkythiolate surfaces showed that solvent trapped close to the interface can be efficient at moving thermal energy away from the surface.¹⁷ Trapped solvent molecules that were orientationally aligned with nearby ligands were able to increase the thermal conductance of the interface. This indicates that the ligand-to-solvent vibrational energy transfer is a key feature for increasing particle-to-solvent thermal conductance.

Recently, we extended RNEMD methods for use in non-periodic geometries by creating scaling/shearing moves between concentric regions of a simulation.²⁰ In this work, we apply this non-periodic variant of RNEMD to investigate the role that *curved* nanoparticle surfaces play in heat and mass transport. On planar surfaces, we discovered that orientational ordering of surface protecting ligands had a large effect on the heat conduction from the metal to the solvent. Smaller nanoparticles have high surface curvature that creates gaps in well-ordered self-assembled monolayers, and the effect of those gaps on the thermal conductance is unknown.

For a solvated nanoparticle, it is possible to define a critical value for the interfacial thermal conductance,

$$G_c = \frac{3C_s\Lambda_s}{RC_p} \quad (1)$$

which depends on the solvent heat capacity, C_s , solvent thermal conductivity, Λ_s , particle radius, R , and nanoparticle heat capacity, C_p .¹ In the limit of infinite interfacial thermal conductance, $G \gg G_c$, cooling of the nanoparticle is limited by the solvent properties, C_s and Λ_s . In the opposite limit, $G \ll G_c$, the heat dissipation is controlled by the thermal conductance of the particle / fluid interface. It is this regime with which we are concerned, where properties of ligands and the particle surface may be tuned to manipulate the rate of cooling for solvated nanoparticles. Based on estimates of G from previous simulations as well as experimental results for solvated nanostructures, gold nanoparticles solvated in hexane are in the $G \ll G_c$ regime for radii smaller than 40 nm. The particles included in this study are more than an order of magnitude smaller than this critical radius, so the heat dissipation should be controlled entirely by the surface features of the particle / ligand / solvent interface.

A. Structures of Self-Assembled Monolayers on Nanoparticles

Though the ligand packing on planar surfaces has been characterized for many different ligands and surface facets, it is not obvious *a priori* how the same ligands will behave on the highly curved surfaces of spherical nanoparticles. Thus, as new applications of ligand-stabilized

nanostructures have been proposed, the structure and dynamics of ligands on metallic nanoparticles have been studied using molecular simulation,²¹ NMR, XPS, FTIR, calorimetry, and surface microscopies.^{22–26} Badia, *et al.* used transmission electron microscopy to determine that alkanethiol ligands on gold nanoparticles pack approximately 30% more densely than on planar Au(111) surfaces.²² Subsequent experiments demonstrated that even at full coverages, surface curvature creates voids between linear ligand chains that can be filled via interdigitation of ligands on neighboring particles.²³ The molecular dynamics simulations of Henz, *et al.* indicate that at low coverages, the thiolate alkane chains will lie flat on the nanoparticle surface²¹ Above 90% coverage, the ligands stand upright and recover the rigidity and tilt angle displayed on planar facets. Their simulations also indicate a high degree of mixing between the thiolate sulfur atoms and surface gold atoms at high coverages.

In this work, thiolated gold nanospheres were modeled using a united atom force field and non-equilibrium molecular dynamics. Gold nanoparticles with radii ranging from 10 - 25 Å were created from a bulk fcc lattice. These particles were passivated with a 50% coverage (compared with the coverage densities reported by Badia *et al.*) of a selection of thiolates. Three straight-chain thiolates of varying chain lengths and rigidities were utilized. These are summarized in Fig. 1. The passivated particles were then solvated in hexane. Details on the united atom force field are given below and in the supporting information.²⁷

II. COMPUTATIONAL DETAILS

A. Creating a thermal flux between particles and solvent

The non-periodic variant of the velocity shearing and scaling RNEMD algorithm (VSS-RNEMD)²⁰ applies a series of velocity scaling and shearing moves at regular intervals to impose a flux between two concentric spherical regions. To impose a thermal flux between the shells (without an accompanying angular shear), we solve for scaling coefficients a and b ,

$$a = \sqrt{1 - \frac{q_r \Delta t}{K_a - K_a^{\text{rot}}}} \tag{2}$$

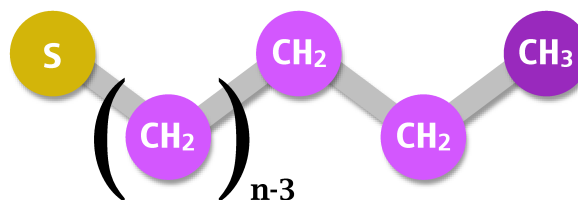
$$b = \sqrt{1 + \frac{q_r \Delta t}{K_b - K_b^{\text{rot}}}} \tag{3}$$

Species

Structure

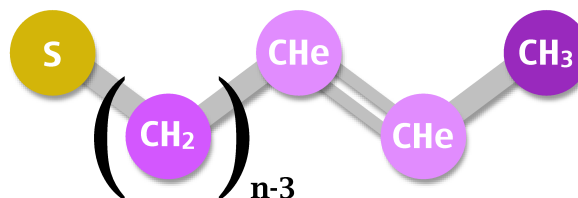
alkanethiolates

$n = 4, 8, 12$



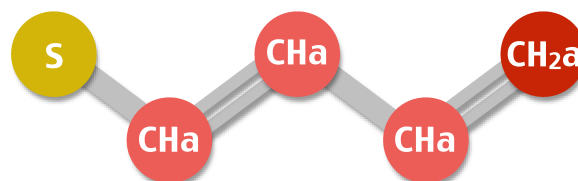
penultimate
alkenethiolates

$n = 4, 8, 12$

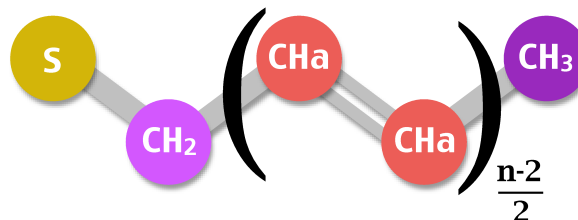


conjugated
alkenethiolates

$n = 4$



$n = 8, 12$



hexane

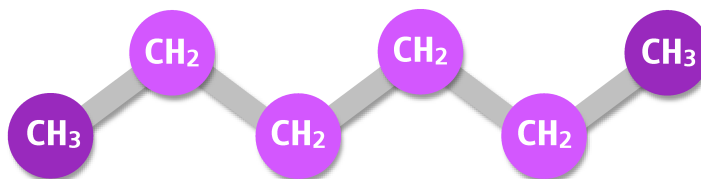


FIG. 1. Topologies of the thiolate capping agents and solvent utilized in the simulations. The chemically-distinct sites (S, CH₂, CH₃, CH_e, CH_a and CH_{2a}) are treated as united atoms. Most parameters are taken from references 28, 29 30. Cross-interactions with the Au atoms were adapted from references 31, 32, and 33.

at each time interval. These scaling coefficients conserve total kinetic energy and angular momentum subject to an imposed heat rate, q_r . The coefficients also depend on the instantaneous kinetic energy, $K_{\{a,b\}}$, and the total rotational kinetic energy of each shell, $K_{\{a,b\}}^{\text{rot}} = \sum_i m_i (\mathbf{v}_i \times \mathbf{r}_i)^2 / 2$.

The scaling coefficients are determined and the velocity changes are applied at regular intervals,

$$\mathbf{v}_i \leftarrow a (\mathbf{v}_i - \langle \omega_a \rangle \times \mathbf{r}_i) + \langle \omega_a \rangle \times \mathbf{r}_i \quad (4)$$

$$\mathbf{v}_j \leftarrow b (\mathbf{v}_j - \langle \omega_b \rangle \times \mathbf{r}_j) + \langle \omega_b \rangle \times \mathbf{r}_j. \quad (5)$$

Here $\langle \omega_a \rangle \times \mathbf{r}_i$ is the contribution to the velocity of particle i due to the overall angular velocity of the a shell. In the absence of an angular momentum flux, the angular velocity $\langle \omega_a \rangle$ of the shell is nearly 0 and the resultant particle velocity is a nearly linear scaling of the initial velocity by the coefficient a or b .

Repeated application of this thermal energy exchange yields a radial temperature profile for the solvated nanoparticles that depends linearly on the applied heat rate, q_r . Similar to the behavior in the slab geometries, the temperature profiles have discontinuities at the interfaces between dissimilar materials. The size of the discontinuity depends on the interfacial thermal conductance, which is the primary quantity of interest.

B. Interfacial Thermal Conductance

As described in earlier work,²⁰ the thermal conductance of each spherical shell may be defined as the inverse Kapitza resistance of the shell. To describe the thermal conductance of an interface of considerable thickness – such as the ligand layers shown here – we can sum the individual thermal resistances of each concentric spherical shell to arrive at the inverse of the total interfacial thermal conductance. In slab geometries, the intermediate temperatures cancel, but for concentric spherical shells, the intermediate temperatures and surface areas remain in the final sum, requiring the use of a series of individual resistance terms:

$$\frac{1}{G} = R_{\text{total}} = \frac{1}{q_r} \sum_i (T_{i+i} - T_i) 4\pi r_i^2. \quad (6)$$

The longest ligand considered here is in excess of 15 Å in length, and we use 10 concentric spherical shells to describe the total interfacial thermal conductance of the ligand layer.

C. Force Fields

Throughout this work, gold – gold interactions are described by the quantum Sutton-Chen (QSC) model.³⁴ Previous work¹⁶ has demonstrated that the electronic contributions to heat conduction (which are missing from the QSC model) across heterogeneous metal / non-metal interfaces are negligible compared to phonon excitation, which is captured by the classical model. The hexane solvent is described by the TraPPE united atom model,²⁸ where sites are located at the carbon centers for alkyl groups. The TraPPE-UA model for hexane provides both computational efficiency and reasonable accuracy for bulk thermal conductivity values. Bonding interactions were used for intra-molecular sites closer than 3 bonds. Effective Lennard-Jones potentials were used for non-bonded interactions.

The TraPPE-UA force field includes parameters for thiol molecules³⁰ as well as unsaturated and aromatic carbon sites.²⁹ These were used for the thiolate molecules in our simulations, and missing parameters for the ligands were supplemented using fits described in the supporting information.²⁷ Bonds are rigid in TraPPE-UA, so although equilibrium bond distances were taken from this force field, flexible bonds were implemented using bond stretching spring constants adapted from the OPLS-AA force field.³⁵

To derive suitable parameters for the thiolates adsorbed on Au(111) surfaces, we adopted the S parameters from Luedtke and Landman³¹ and modified the parameters for the CTS atom to maintain charge neutrality in the molecule.

Other interactions between metal (Au) and non-metal atoms were adapted from an adsorption study of alkyl thiols on gold surfaces by Vlugt, *et al.*³² They fit an effective pair-wise Lennard-Jones form of potential parameters for the interaction between Au and pseudo-atoms CH_x and S based on a well-established and widely-used effective potential of Hautman and Klein for the Au(111) surface.³³

All additional terms to represent thiolated alkenes and conjugated ligand moieties were parameterized as part of this work and are available in the supporting information.²⁷ All simulations were carried out with the open source molecular dynamics package, OpenMD.^{36,37}

D. Simulation Protocol

Gold nanospheres with radii ranging from 10 - 25 Å were created from a bulk fcc lattice and were thermally equilibrated prior to the addition of ligands. A 50% coverage of ligands (based on coverages reported by Badia, *et al.*²²) was placed on the surface of the equilibrated nanoparticles using Packmol³⁸. We have chosen three lengths for the straight-chain ligands, C_4 , C_8 , and C_{12} , differentiated by the number of carbons in the chains. Additionally, to explore the effects of ligand flexibility, we have used three levels of ligand “stiffness”. The most flexible chain is a fully saturated alkanethiolate, while moderate rigidity is introduced using an alkene thiolate with one double bond in the penultimate (solvent-facing) carbon-carbon location. The most rigid ligands are fully-conjugated chains where all of the carbons are represented with conjugated (aryl) united-atom carbon atoms (CHar or terminal CH_2ar).

The nanoparticle / ligand complexes were thermally equilibrated to allow for ligand conformational flexibility. Packmol was then used to solvate the structures inside a spherical droplet of hexane. The thickness of the solvent layer was chosen to be at least $1.5\times$ the combined radius of the nanoparticle / ligand structure. The fully solvated system was equilibrated for at least 1 ns using the “Langevin Hull” algorithm to apply 50 atm of pressure and a target temperature of 250 K.³⁹ Typical system sizes ranged from 18,310 united atom sites for the 10 Å particles with C_4 ligands to 89,490 sites for the 25 Å particles with C_{12} ligands. Figure 2 shows one of the solvated 25 Å nanoparticles passivated with the C_{12} alkane thiolate ligands.

Once equilibrated, thermal fluxes were applied for 1 ns, until stable temperature gradients had developed (see figure 3). Systems were run under moderate pressure (50 atm) with an average temperature (250K) that maintained a compact solvent cluster and avoided formation of a vapor layer near the heated metal surface. Pressure was applied to the system via the non-periodic “Langevin Hull” algorithm.³⁹ However, thermal coupling to the external temperature bath was removed to avoid interference with the imposed RNEMD flux.

Although the VSS-RNEMD moves conserve *total* angular momentum and energy, systems which contain a metal nanoparticle embedded in a significant volume of solvent will still experience nanoparticle diffusion inside the solvent droplet. To aid in measuring an accurate temperature profile for these systems, a single gold atom at the origin of the coordinate system was assigned a mass $10,000\times$ its original mass. The bonded and nonbonded interactions for this atom remain unchanged and the heavy atom is excluded from the RNEMD velocity scaling. The only effect of

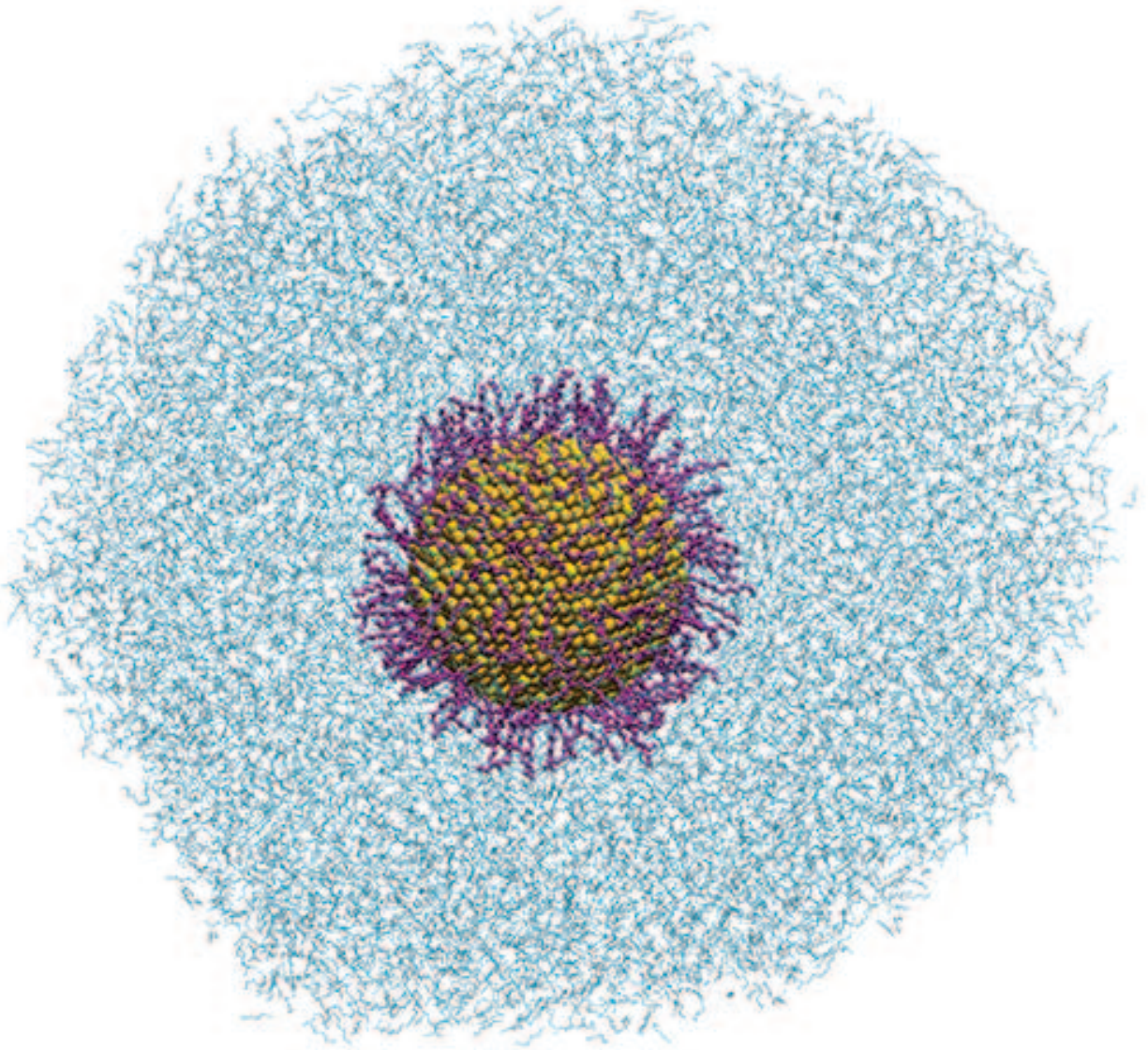


FIG. 2. A 25 Å radius gold nanoparticle protected with a half-monolayer of TraPPE-UA dodecanethiolate (C_{12}) ligands and solvated in TraPPE-UA hexane. The interfacial thermal conductance is computed by applying a kinetic energy flux between the nanoparticle and an outer shell of solvent.

this gold atom is to effectively pin the nanoparticle at the origin of the coordinate system, thereby preventing translational diffusion of the nanoparticle due to Brownian motion.

To provide statistical independence, five separate configurations were simulated for each particle radius and ligand. The structures were unique, starting at the point of ligand placement, in order to sample multiple surface-ligand configurations.

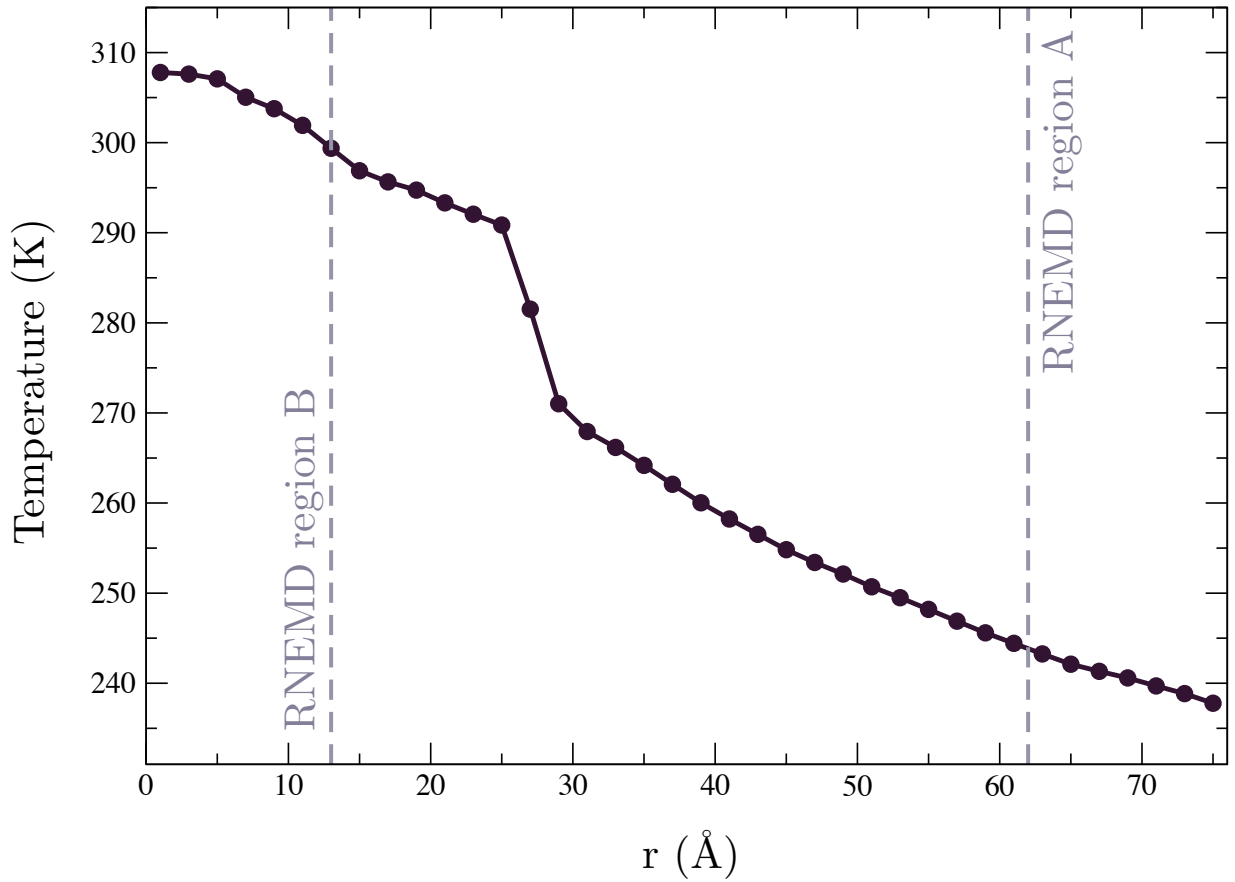


FIG. 3. Radial temperature profile for a 25 Å radius particle protected with a 50% coverage of TraPPE-UA butanethiolate (C_4) ligands and solvated in TraPPE-UA hexane. A kinetic energy flux is applied between RNEMD region A and RNEMD region B. The size of the temperature discontinuity at the interface is governed by the interfacial thermal conductance.

III. RESULTS

We modeled four sizes of nanoparticles ($R = 10, 15, 20,$ and 25 \AA). The smallest particle size produces the lowest interfacial thermal conductance values for most of the protecting groups (Fig. 4). Between the other three sizes of nanoparticles, there is no systematic dependence of the interfacial thermal conductance on the nanoparticle size. It is likely that the differences in local curvature of the nanoparticle sizes studied here do not disrupt the ligand packing and behavior in drastically different ways.

Unlike our previous study of varying thiolate ligand chain lengths on planar Au(111) surfaces,

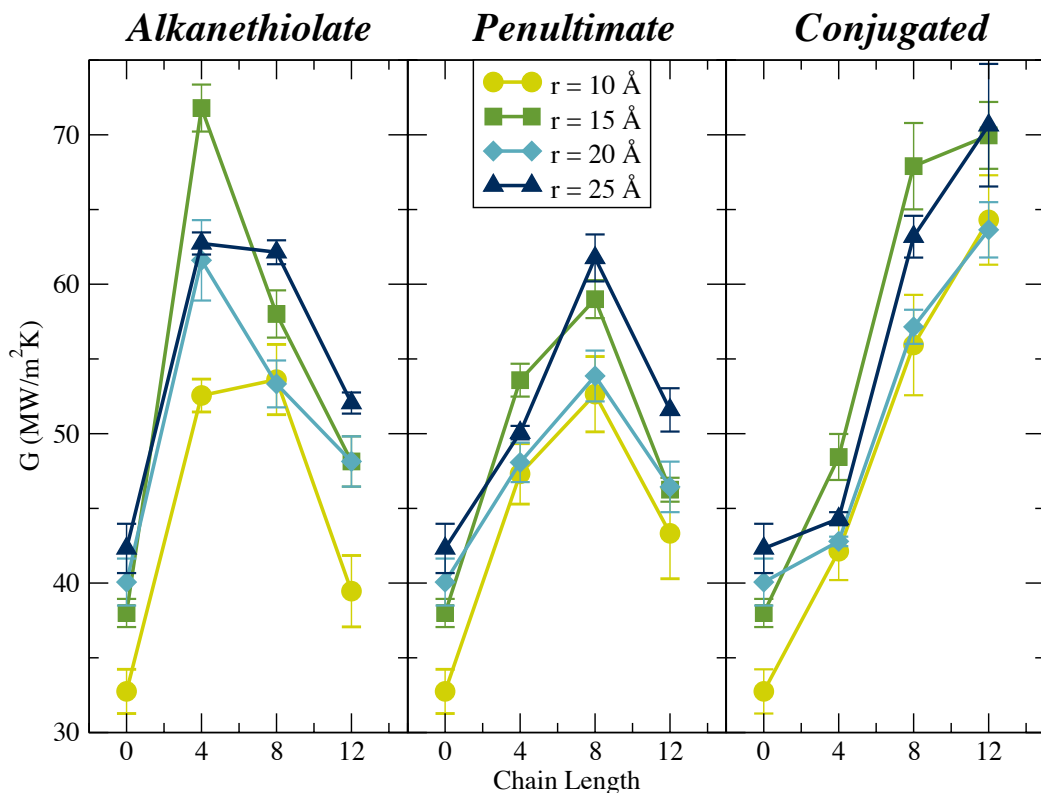


FIG. 4. Interfacial thermal conductance (G) values for 4 sizes of solvated nanoparticles that are bare or protected with a 50% coverage of C_4 , C_8 , or C_{12} thiolate ligands. Ligands of different flexibility are shown in separate panels. The middle panel indicates ligands which have a single carbon-carbon double bond in the penultimate position.

the interfacial thermal conductance of ligand-protected nanospheres exhibits a distinct dependence on the ligand identity. A half-monolayer coverage of ligands yields interfacial conductance that is strongly dependent on both ligand length and flexibility.

There are many factors that could be playing a role in the ligand-dependent conductance. The sulfur-gold interaction is particularly strong, and the presence of the ligands can easily disrupt the crystalline structure of the gold at the surface of the particles, providing more efficient scattering of phonons into the ligand / solvent layer. This effect would be particularly important at small particle sizes.

In previous studies of mixed-length ligand layers with full coverage, we observed that ligand-

solvent alignment was an important factor for heat transfer into the solvent. With high surface curvature and lower effective coverages, ligand behavior also becomes more complex. Some chains may be lying down on the surface, and solvent may not be penetrating the ligand layer to the same degree as in the planar surfaces.

Additionally, the ligand flexibility directly alters the vibrational density of states for the layer that mediates the transfer of phonons between the metal and the solvent. This could be a partial explanation for the observed differences between the fully conjugated and more flexible ligands.

In the following sections we provide details on how we measure surface corrugation, solvent-ligand interpenetration, and ordering of the solvent and ligand at the surfaces of the nanospheres. We also investigate the overlap between vibrational densities of states for the various ligands.

A. Corrugation of the Particle Surface

The bonding sites for thiols on gold surfaces have been studied extensively and include configurations beyond the traditional atop, bridge, and hollow sites found on planar surfaces. In particular, the deep potential well between the gold atoms and the thiolate sulfur atoms leads to insertion of the sulfur into the gold lattice and displacement of interfacial gold atoms. The degree of ligand-induced surface restructuring may have an impact on the interfacial thermal conductance and is an important phenomenon to quantify.

Henz, *et al.*²¹ used the metal density as a function of radius to measure the degree of mixing between the thiol sulfurs and surface gold atoms at the edge of a nanoparticle. Although metal density is important, disruption of the local crystalline ordering would also have a large effect on the phonon spectrum in the particles. To measure this effect, we use the fraction of gold atoms exhibiting local fcc ordering as a function of radius to describe the ligand-induced disruption of the nanoparticle surface.

The local bond orientational order can be described using the method of Steinhardt *et al.*⁴⁰ The local bonding environment, $\bar{q}_{\ell m}$, for each atom in the system is determined by averaging over the spherical harmonics between that atom and each of its neighbors,

$$\bar{q}_{\ell m} = \sum_i Y_{\ell}^m(\theta_i, \phi_i) \tag{7}$$

where θ_i and ϕ_i are the relative angular coordinates of neighbor i in the laboratory frame. A global average orientational bond order parameter, $\bar{Q}_{\ell m}$, is the average over each $\bar{q}_{\ell m}$ for all atoms in the

system. To remove the dependence on the laboratory coordinate frame, the third order rotationally invariant combination of $\bar{Q}_{\ell m}$, \hat{w}_ℓ , is utilized here.^{40,41}

For $\ell = 4$, the ideal face-centered cubic (fcc), body-centered cubic (bcc), hexagonally close-packed (hcp), and simple cubic (sc) local structures exhibit \hat{w}_4 values of -0.159, 0.134, 0.159, and 0.159, respectively. Because \hat{w}_4 exhibits an extreme value for fcc structures, it is ideal for measuring local fcc ordering. The spatial distribution of \hat{w}_4 local bond orientational order parameters, $p(\hat{w}_4, r)$, can provide information about the location of individual atoms that are central to local fcc ordering.

The fraction of fcc-ordered gold atoms at a given radius in the nanoparticle,

$$f_{\text{fcc}}(r) = \int_{-\infty}^{w_c} p(\hat{w}_4, r) d\hat{w}_4 \quad (8)$$

is described by the distribution of the local bond orientational order parameters, $p(\hat{w}_4, r)$, and w_c , a cutoff for the peak \hat{w}_4 value displayed by fcc structures. A w_c value of -0.12 was chosen to isolate the fcc peak in \hat{w}_4 .

As illustrated in Figure 5, the presence of ligands decreases the fcc ordering of the gold atoms at the nanoparticle surface. For the smaller nanoparticles, this disruption extends into the core of the nanoparticle, indicating widespread disruption of the lattice.

We may describe the thickness of the disrupted nanoparticle surface by defining a corrugation factor, c , as the ratio of the radius at which the fraction of gold atoms with fcc ordering is 0.9 and the radius at which the fraction is 0.5.

$$c = 1 - \frac{r(f_{\text{fcc}} = 0.9)}{r(f_{\text{fcc}} = 0.5)} \quad (9)$$

A sharp interface will have a steep drop in f_{fcc} at the edge of the particle ($c \rightarrow 0$). In the opposite limit where the entire nanoparticle surface is restructured by ligands, the radius at which there is a high probability of fcc ordering moves dramatically inward ($c \rightarrow 1$).

The computed corrugation factors are shown in Figure 6 for bare nanoparticles and for ligand-protected particles as a function of ligand chain length. The largest nanoparticles are only slightly restructured by the presence of ligands on the surface, while the smallest particle ($r = 10 \text{ \AA}$) exhibits significant disruption of the original fcc ordering when covered with a half-monolayer of thiol ligands.

Because the thiolate ligands do not significantly alter the larger particle crystallinity, the surface corrugation does not seem to be a likely candidate to explain the large increase in thermal

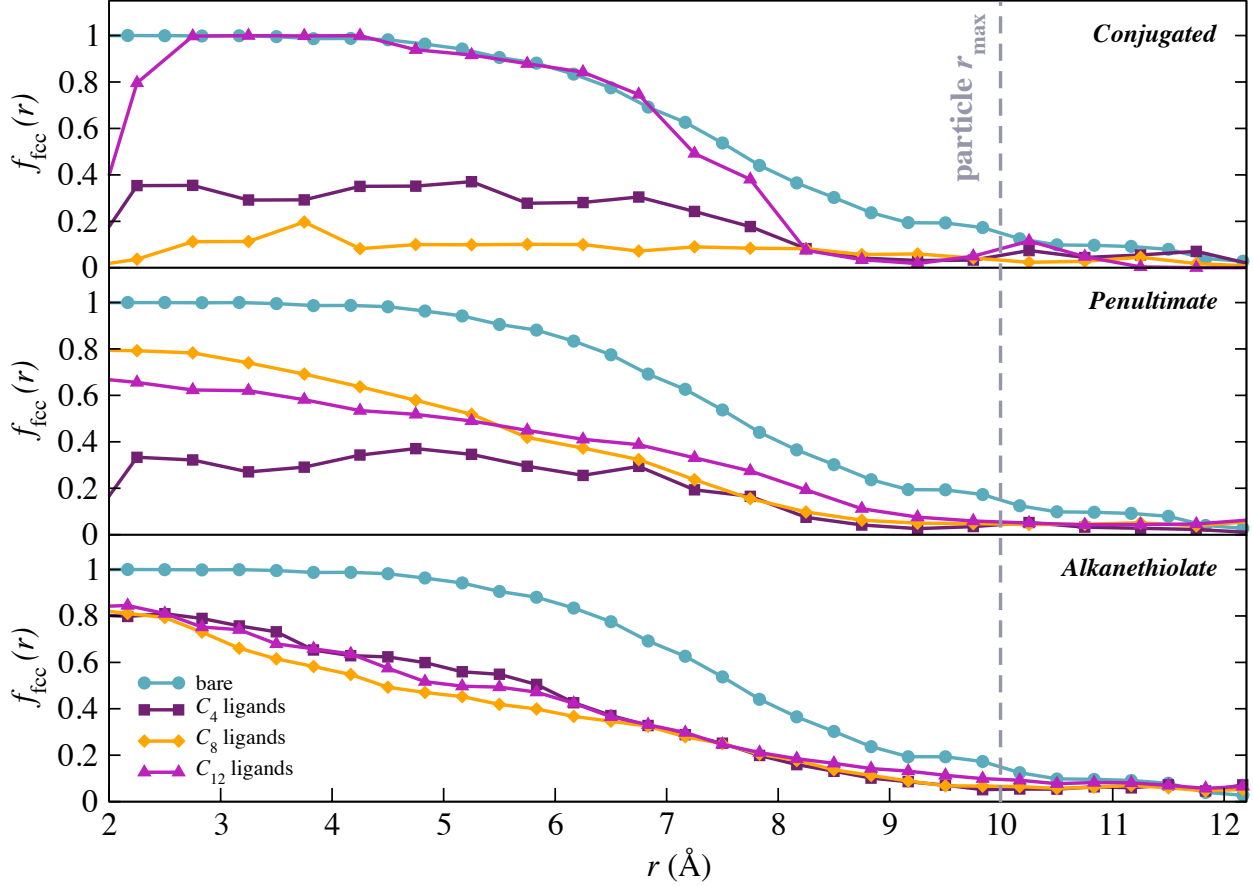


FIG. 5. Fraction of gold atoms with fcc ordering as a function of radius for a 10 Å radius nanoparticle. The decreased fraction of fcc-ordered atoms in ligand-protected nanoparticles relative to bare particles indicates restructuring of the nanoparticle surface by the thiolate sulfur atoms.

conductance at the interface when ligands are added.

B. Orientation of Ligand Chains

Previous theoretical work on heat conduction through alkane chains has shown that short chains are dominated by harmonic interactions, where the energy is carried ballistically through the chain.⁴² As the saturated ligand chain length increases in length, it exhibits significantly more conformational flexibility. Thus, different lengths of ligands should favor different chain orientations on the surface of the nanoparticle, and can localize the ligand vibrational density of states close to the particle, lowering the effectiveness of the heat conduction.⁴² To determine the distribution of ligand orientations relative to the particle surface we examine the probability of finding

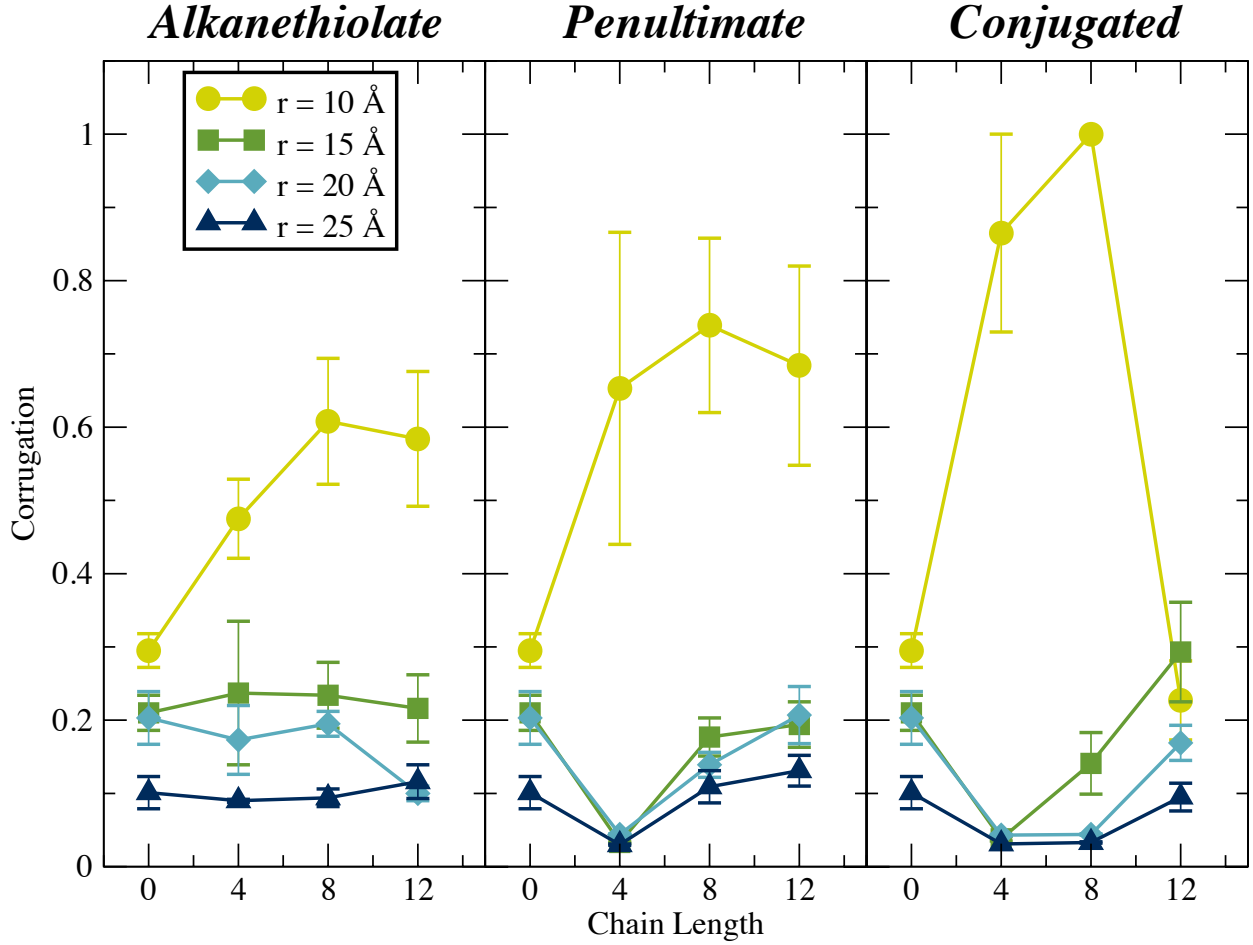


FIG. 6. Computed corrugation values for 4 sizes of solvated nanoparticles that are bare or protected with a 50% coverage of C_4 , C_8 , or C_{12} thiolate ligands. The smallest (10 Å) particles show significant disruption to their crystal structures, and the length and stiffness of the ligands is a contributing factor to the surface disruption.

a ligand with a particular orientation relative to the surface normal of the nanoparticle,

$$\cos(\theta) = \frac{\vec{r}_i \cdot \hat{u}_i}{|\vec{r}_i| |\hat{u}_i|} \quad (10)$$

where \vec{r}_i is the vector between the cluster center of mass and the sulfur atom on ligand molecule i , and \hat{u}_i is the vector between the sulfur atom and CH_3 pseudo-atom on ligand molecule i . As depicted in Figure 7, $\theta \rightarrow 180^\circ$ for a ligand chain standing upright on the particle ($\cos(\theta) \rightarrow -1$) and $\theta \rightarrow 90^\circ$ for a ligand chain lying down on the surface ($\cos(\theta) \rightarrow 0$). As the thiolate alkane chain increases in length and becomes more flexible, the ligands are more willing to lie down on the nanoparticle surface and exhibit increased population at $\cos(\theta) = 0$.

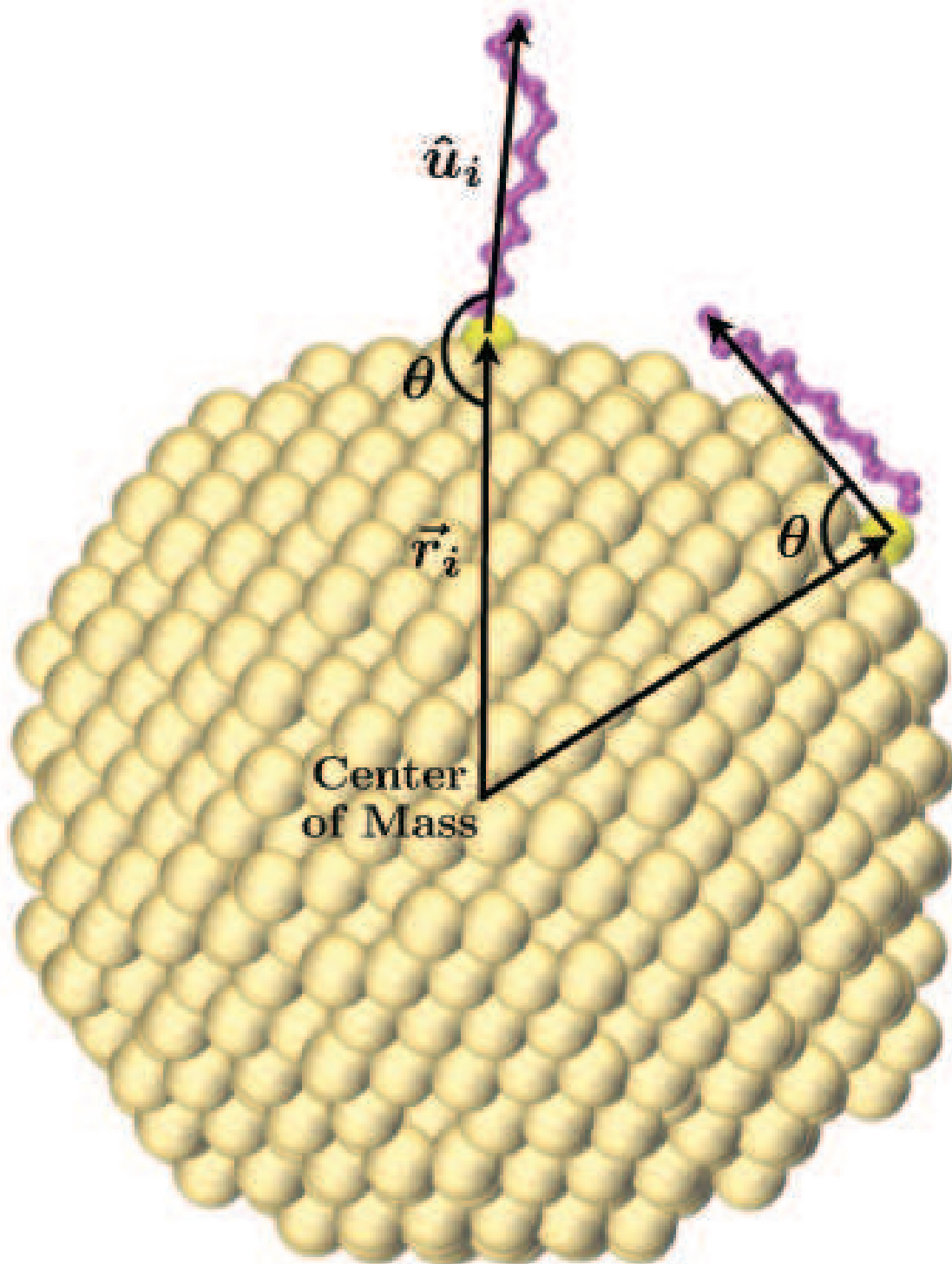


FIG. 7. The two extreme cases of ligand orientation relative to the nanoparticle surface: the ligand completely outstretched ($\cos(\theta) = -1$) and the ligand fully lying down on the particle surface ($\cos(\theta) = 0$).

An order parameter describing the average ligand chain orientation relative to the nanoparticle surface is available using the second order Legendre parameter,

$$P_2 = \left\langle \frac{1}{2} (3 \cos^2(\theta) - 1) \right\rangle \quad (11)$$

Ligand populations that are perpendicular to the particle surface have P_2 values of 1, while ligand populations lying flat on the nanoparticle surface have P_2 values of -0.5 . Disordered ligand layers will exhibit mean P_2 values of 0. As shown in Figure 8 the ligand P_2 values approaches 0 as ligand chain length – and ligand flexibility – increases.

C. Orientation of Interfacial Solvent

Similarly, we examined the distribution of *hexane* molecule orientations relative to the particle surface using the same angular analysis utilized for the ligand chain orientations. In this case, \vec{r}_i is the vector between the particle center of mass and one of the CH_2 pseudo-atoms in the middle of hexane molecule i and \hat{u}_i is the vector between the two CH_3 pseudo-atoms on molecule i . Since we are only interested in the orientation of solvent molecules near the ligand layer, we select only the hexane molecules within a specific r -range, between the edge of the particle and the end of the ligand chains. A large population of hexane molecules with $\cos(\theta) \sim \pm 1$ would indicate interdigitation of the solvent molecules between the upright ligand chains. A more random distribution of $\cos(\theta)$ values indicates a disordered arrangement of solvent molecules near the particle surface. Again, P_2 order parameter values provide a population analysis for the solvent that is close to the particle surface.

The average orientation of the interfacial solvent molecules is notably flat on the *bare* nanoparticle surfaces. This blanket of hexane molecules on the particle surface may act as an insulating layer, increasing the interfacial thermal resistance. As the length (and flexibility) of the ligand increases, the average interfacial solvent P_2 value approaches 0, indicating a more random orientation of the ligand chains. The average orientation of solvent within the C_8 and C_{12} ligand layers is essentially random. Solvent molecules in the interfacial region of C_4 ligand-protected nanoparticles do not lie as flat on the surface as in the case of the bare particles, but are not as randomly oriented as the longer ligand lengths.

These results are particularly interesting in light of our previous results¹⁷, where solvent molecules readily filled the vertical gaps between neighboring ligand chains and there was a

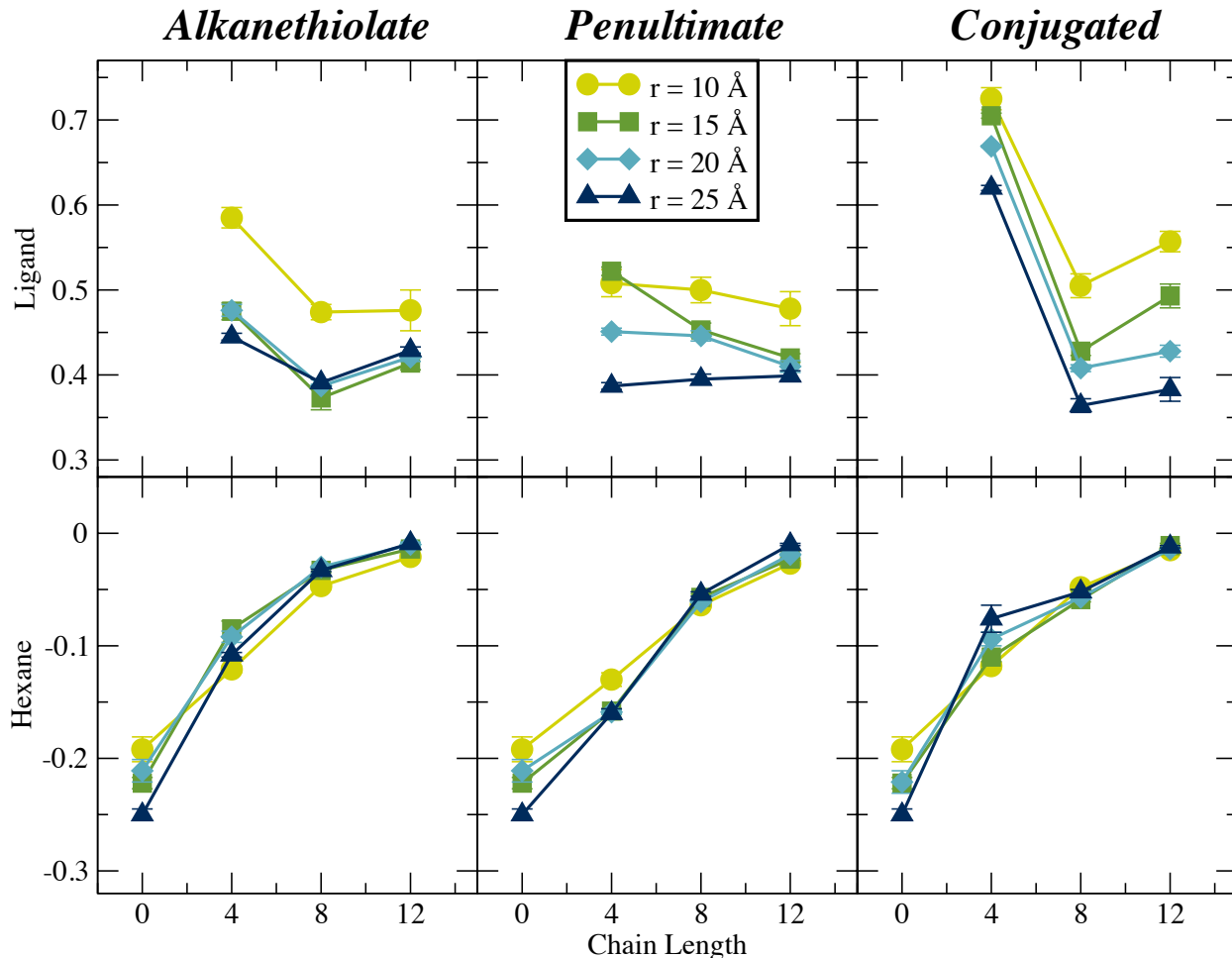


FIG. 8. Computed ligand and interfacial solvent orientational P_2 values for 4 sizes of solvated nanoparticles that are bare or protected with a 50% coverage of C₄, C₈, or C₁₂ alkanethiolate ligands. Increasing stiffness of the ligand orients these molecules normal to the particle surface, while the length of the ligand chains works to prevent solvent from lying flat on the surface.

strong correlation between ligand and solvent molecular orientations. It appears that the introduction of surface curvature and a lower ligand packing density creates a disordered ligand layer that lacks well-formed channels for the solvent molecules to occupy.

D. Solvent Penetration of Ligand Layer

The extent of ligand – solvent interaction is also determined by the degree to which these components occupy the same region of space adjacent to the nanoparticle. The radial density profiles of these components help determine this degree of interaction. Figure 9 shows representative den-

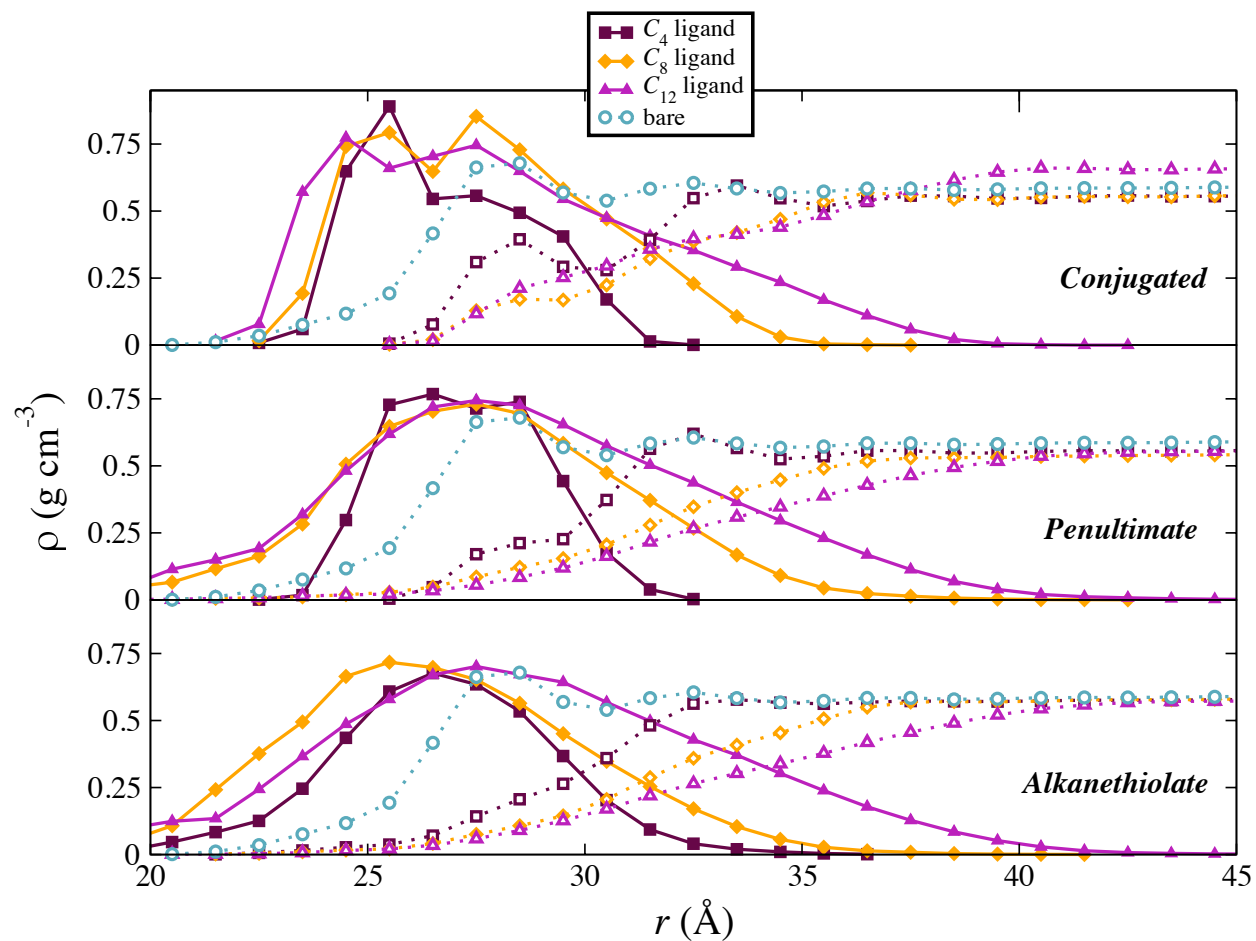


FIG. 9. Radial density profiles for 25 Å radius nanoparticles with no ligands (circles), C_4 ligands (squares), C_8 ligands (diamonds), and C_{12} ligands (triangles). Ligand density is indicated with filled symbols, solvent (hexane) density is indicated with open symbols. As ligand chain length increases, the nearby solvent is excluded from the ligand layer. The conjugated ligands (upper panel) can create a separated solvent shell within the ligand layer and also allow significantly more solvent to penetrate close to the particle.

sity profiles for solvated 25 Å radius nanoparticles with no ligands, and with a 50% coverage of C_4 , C_8 , and C_{12} thiolates.

The differences between the radii at which the hexane surrounding the ligand-covered particles reaches bulk density correspond nearly exactly to the differences between the lengths of the ligand chains. Beyond the edge of the ligand layer, the solvent reaches its bulk density within a few angstroms. The differing shapes of the density curves indicate that the solvent is increasingly excluded from the ligand layer as the chain length increases.

The conjugated ligands create a distinct solvent shell within the ligand layer and also allow

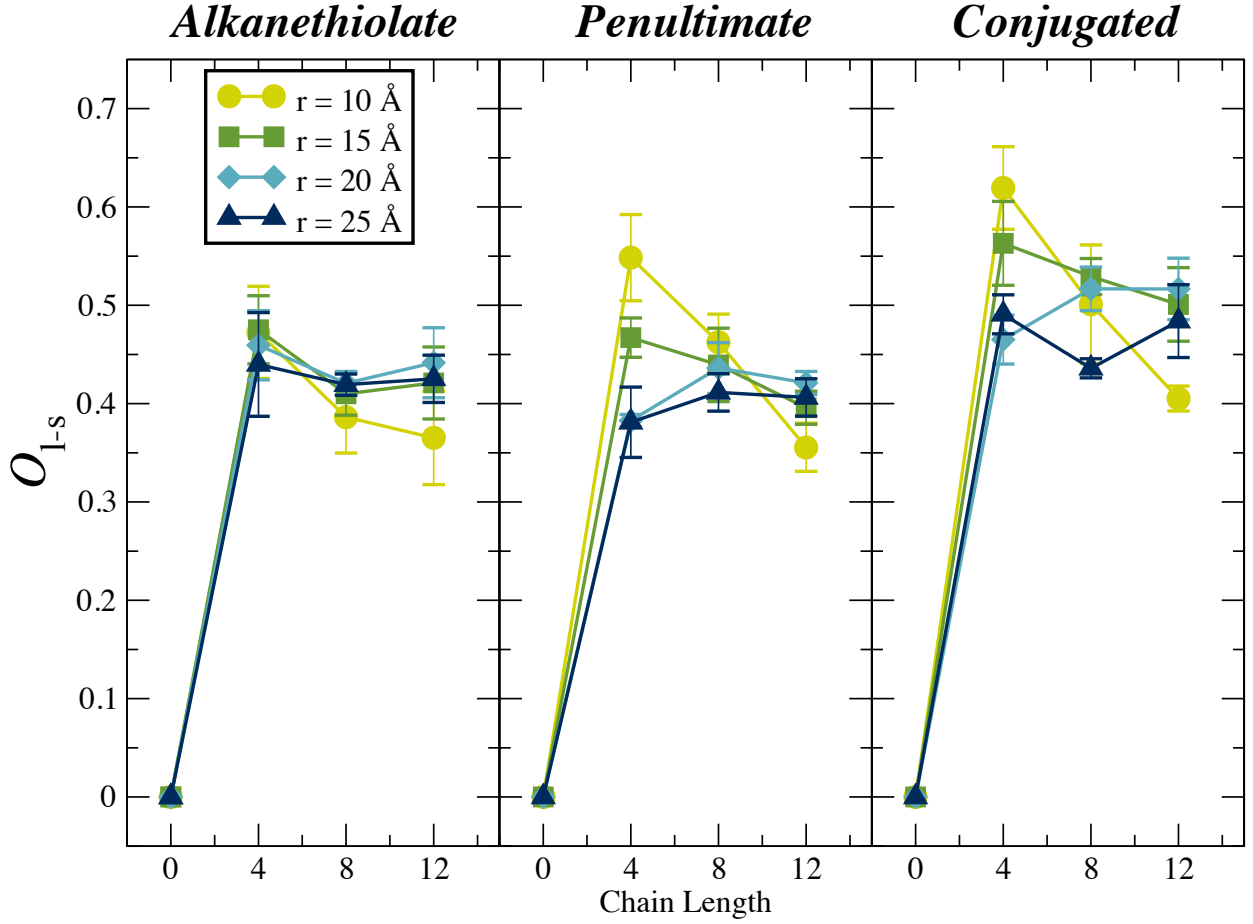


FIG. 10. Density overlap parameters (O_{l-s}) for solvated nanoparticles protected by thiolate ligands. In general, the rigidity of the fully-conjugated ligands provides the easiest route for solvent to enter the interfacial region. Additionally, shorter chains allow a greater degree of solvent penetration of the ligand layer.

significantly more solvent to penetrate close to the particle. We define a density overlap parameter,

$$O_{l-s} = \frac{1}{V} \int_0^{r_{\max}} 4\pi r^2 \frac{4\rho_l(r)\rho_s(r)}{(\rho_l(r) + \rho_s(r))^2} dr \quad (12)$$

where $\rho_l(r)$ and $\rho_s(r)$ are the ligand and solvent densities at a radius r , and V is the total integration volume ($V = 4\pi r_{\max}^3/3$). The fraction in the integrand is a dimensionless quantity that is unity when ligand and solvent densities are identical at radius r , but falls to zero when either of the two components are excluded from that region.

The density overlap parameters are shown in Fig. 10. The calculated overlap parameters indicate that the conjugated ligand allows for the most solvent penetration close to the particle, and that shorter chains generally permit greater solvent penetration in the interfacial region. Increasing overlap can certainly allow for enhanced thermal transport, but this is clearly not the only

contributing factor. Even when the solvent and ligand are in close physical contact, there must also be good vibrational overlap between the phonon densities of states in the ligand and solvent to transmit vibrational energy between the two materials.

E. Ligand-mediated Vibrational Overlap

In phonon scattering models for interfacial thermal conductance,^{9,43–46} the frequency-dependent transmission probability ($t_{a \rightarrow b}(\omega)$) predicts phonon transfer between materials a and b . Many of the models for interfacial phonon transmission estimate this quantity using the phonon density of states and group velocity, and make use of a Debye model for the density of states in the solid.

A consensus picture is that in order to transfer the energy carried by an incoming phonon of frequency ω on the a side, the phonon density of states on the b side must have a phonon of the same frequency. The overlap of the phonon densities of states, particularly at low frequencies, therefore contributes to the transfer of heat. Phonon scattering must also be done in a direction perpendicular to the interface. In the geometries described here, there are two interfaces (particle \rightarrow ligand, and ligand \rightarrow solvent), and the vibrational overlap between the ligand and the other two components is going to be relevant to heat transfer.

To estimate the relevant densities of states, we have projected the velocity of each atom i in the region of the interface onto a direction normal to the interface. For the nanosphere geometries studied here, the normal direction depends on the instantaneous position of the atom relative to the center of mass of the particle.

$$v_{\perp}(t) = \mathbf{v}(t) \cdot \frac{\mathbf{r}(t)}{|\mathbf{r}(t)|} \quad (13)$$

The quantity $v_{\perp}(t)$ measures the instantaneous velocity of an atom in a direction perpendicular to the nanoparticle interface. In the interfacial region, the autocorrelation function of these velocities,

$$C_{\perp}(t) = \langle v_{\perp}(t) \cdot v_{\perp}(0) \rangle, \quad (14)$$

will include contributions from all of the phonon modes present at the interface. The Fourier transform of the time-symmetrized autocorrelation function provides an estimate of the vibrational density of states,⁴⁷

$$\rho(\omega) = \frac{1}{\tau} \int_{-\tau/2}^{\tau/2} C_{\perp}(t) e^{-i\omega t} dt. \quad (15)$$

Here τ is the total observation time for the autocorrelation function. In Fig. 11 we show the low-frequency region of the normalized vibrational densities of states for the three chemical compo-

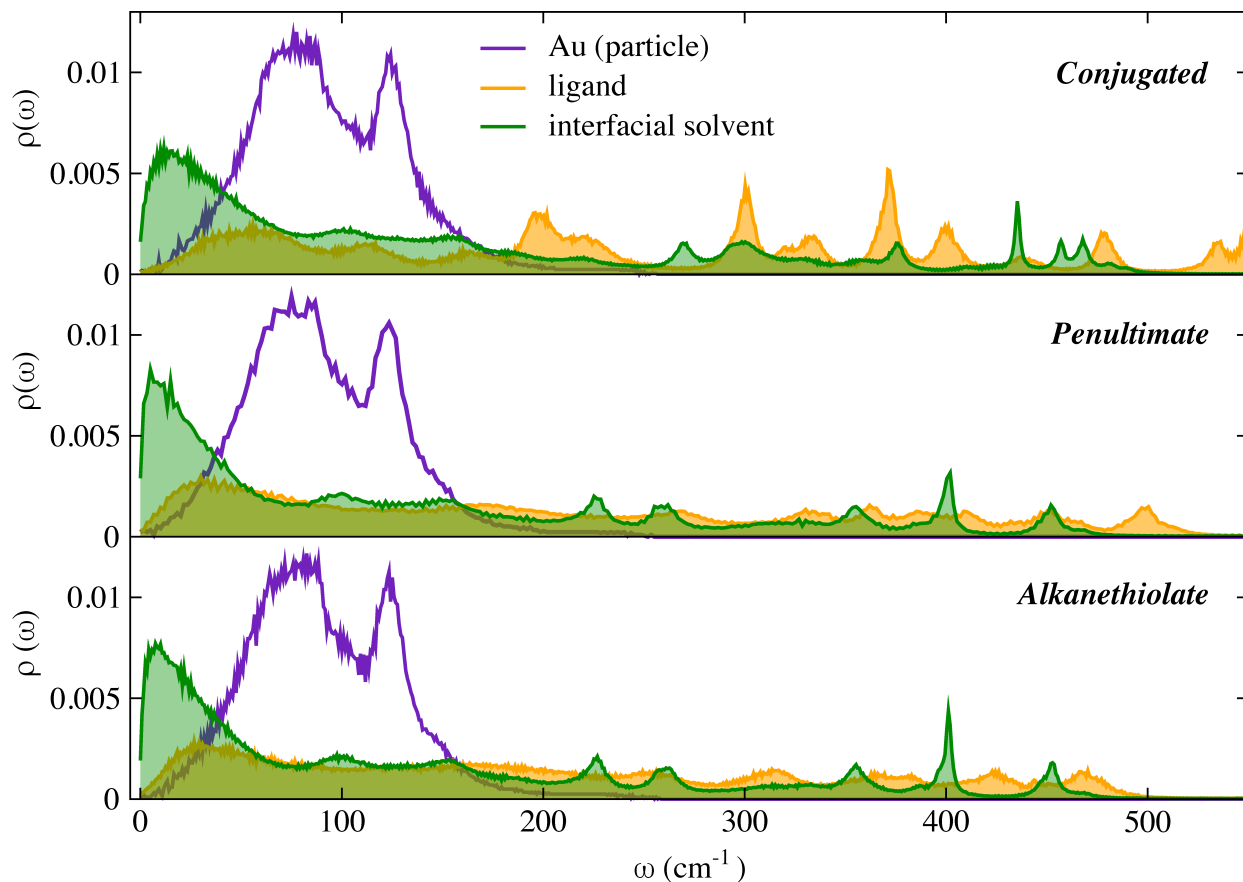


FIG. 11. The low frequency portion of the vibrational density of states for three chemical components (gold nanoparticles, C_{12} ligands, and hexane solvent). These densities of states were computed using the velocity autocorrelation functions for atoms in the interfacial region, constructed with velocities projected onto a direction normal to the interface.

nents (gold nanoparticle, C_{12} ligands, and interfacial solvent). The double bond in the penultimate location is a small perturbation on ligands of this size, and that is reflected in relatively similar spectra in the lower panels. The fully conjugated ligand, however, pushes the peak in the lowest frequency band from $\sim 29\text{cm}^{-1}$ to $\sim 55\text{cm}^{-1}$, yielding significant overlap with the density of states in the nanoparticle. This ligand also increases the overlap with the solvent density of states in a band between 280 and 380cm^{-1} . This provides some physical basis for the high interfacial conductance observed for the fully conjugated C_8 and C_{12} ligands.

The similarity between the density of states for the alkanethiolate and penultimate ligands also helps explain why the interfacial conductance is nearly the same for these two ligands, particularly at longer chain lengths.

IV. DISCUSSION

The chemical bond between the metal and the ligand introduces vibrational overlap that is not present between the bare metal surface and solvent. Thus, regardless of ligand identity or chain length, the presence of a half-monolayer ligand coverage yields a higher interfacial thermal conductance value than the bare nanoparticle. The mechanism for the varying conductance for the different ligands is somewhat less clear. Ligand-based alterations to vibrational density of states is a major contributor, but some of the ligands can disrupt the crystalline structure of the smaller nanospheres, while others can re-order the interfacial solvent and alter the interpenetration profile between ligand and solvent chains. Further work to separate the effects of ligand-solvent interpenetration and surface reconstruction is clearly needed for a complete picture of the heat transport in these systems.

ACKNOWLEDGMENTS

Support for this project was provided by the National Science Foundation under grant CHE-1362211. Computational time was provided by the Center for Research Computing (CRC) at the University of Notre Dame.

REFERENCES

- ¹O. Wilson, X. Hu, D. Cahill, and P. Braun, *Phys. Rev. B* **66**, 224301 (2002).
- ²Z. Ge, D. G. Cahill, and P. V. Braun, *J. Phys. Chem. B* **108**, 18870 (2004), <http://pubs.acs.org/doi/pdf/10.1021/jp048375k>.
- ³N. Shenogina, R. Godawat, P. Keblinski, and S. Garde, *Phys. Rev. Lett.* **102**, 156101 (2009).
- ⁴Z. Wang, J. A. Carter, A. Lagutchev, Y. K. Koh, N.-H. Seong, D. G. Cahill, and D. D. Dlott, *Science* **317**, 787 (2007), <http://www.sciencemag.org/content/317/5839/787.full.pdf>.
- ⁵A. J. Schmidt, J. D. Alper, M. Chiesa, G. Chen, S. K. Das, and K. Hamad-Schifferli, *J. Phys. Chem. C* **112**, 13320 (2008), <http://pubs.acs.org/doi/pdf/10.1021/jp8051888>.
- ⁶V. Juvé, M. Scardamaglia, P. Maioli, A. Crut, S. Merabia, L. Joly, N. Del Fatti, and F. Vallée, *Phys. Rev. B* **80**, 195406 (2009).
- ⁷J. Alper and K. Hamad-Schifferli, *Langmuir* **26**, 3786 (2010), <http://pubs.acs.org/doi/pdf/10.1021/la904855s>.
- ⁸H. Harikrishna, W. A. Ducker, and S. T. Huxtable, *Appl. Phys. Lett.* **102**, 251606 (2013).
- ⁹D. G. Cahill, W. K. Ford, K. E. Goodson, G. D. Mahan, A. Majumdar, H. J. Maris, R. Merlin, and S. R. Phillpot, *J. Appl. Phys.* **93**, 793 (2003).
- ¹⁰M. D. Losego, M. E. Grady, N. R. Sottos, D. G. Cahill, and P. V. Braun, *Nat Mater* **11**, 502 (2012).
- ¹¹W.-L. Ong, S. M. Rupich, D. V. Talapin, A. J. H. McGaughey, and J. A. Malen, *Nat Mater* **12**, 410 (2013).
- ¹²W.-L. Ong, S. Majumdar, J. A. Malen, and A. J. H. McGaughey, *J. Phys. Chem. C* **118**, 7288 (2014), <http://dx.doi.org/10.1021/jp4120157>.
- ¹³J. Soussi, S. Volz, B. Palpant, and Y. Chalopin, *Appl. Phys. Lett.* **106**, 093113 (2015), <http://dx.doi.org/10.1063/1.4913905>.
- ¹⁴Z. Ge, D. G. Cahill, and P. V. Braun, *Phys. Rev. Lett.* **96**, 186101 (2006).
- ¹⁵G. Kikugawa, T. Ohara, T. Kawaguchi, E. Torigoe, Y. Hagiwara, and Y. Matsumoto, *J. Chem. Phys.* **130**, 074706 (2009).
- ¹⁶S. Kuang and J. D. Gezelter, *J. Phys. Chem. C* **115**, 22475 (2011), <http://pubs.acs.org/doi/pdf/10.1021/jp2073478>.
- ¹⁷K. M. Stocker and J. D. Gezelter, *J. Phys. Chem. C* **117**, 7605 (2013), <http://pubs.acs.org/doi/pdf/10.1021/jp312734f>.

- ¹⁸Z. Tian, A. Marconnet, and G. Chen, *Appl. Phys. Lett.* **106**, 211602 (2015).
- ¹⁹F. Müller-Plathe, *J. Chem. Phys.* **106**, 6082 (1997).
- ²⁰K. M. Stocker and J. D. Gezelter, *J. Chem. Theory Comput.* **10**, 1878 (2014), <http://pubs.acs.org/doi/pdf/10.1021/ct500221u>.
- ²¹B. J. Henz, T. Hawa, and M. R. Zachariah, *Langmuir* **24**, 773 (2008), <http://pubs.acs.org/doi/pdf/10.1021/la7024473>.
- ²²A. Badia, S. Singh, L. Demers, L. Cuccia, G. R. Brown, and R. B. Lennox, *Chem. Eur. J.* **2**, 359 (1996).
- ²³A. Badia, W. Gao, S. Singh, L. Demers, L. Cuccia, and L. Reven, *Langmuir* **12**, 1262 (1996).
- ²⁴A. Badia, L. Demers, L. Dickinson, F. G. Morin, R. B. Lennox, and L. Reven, *J. Am. Chem. Soc.* **119**, 11104 (1997), <http://pubs.acs.org/doi/pdf/10.1021/ja9726163>.
- ²⁵A. Badia, L. Cuccia, L. Demers, F. Morin, and R. B. Lennox, *J. Am. Chem. Soc.* **119**, 2682 (1997), <http://pubs.acs.org/doi/pdf/10.1021/ja963571t>.
- ²⁶A. Badia, R. B. Lennox, and L. Reven, *Acc. Chem. Res.* **33**, 475 (2000).
- ²⁷See supplemental material for more details on the force field used for these simulations..
- ²⁸M. G. Martin and J. I. Siepmann, *J. Phys. Chem. B* **102**, 2569 (1998).
- ²⁹C. D. Wick, M. G. Martin, and J. I. Siepmann, *J. Phys. Chem. B* **104**, 8008 (2000), <http://pubs.acs.org/doi/pdf/10.1021/jp001044x>.
- ³⁰N. Lubna, G. Kamath, J. J. Potoff, N. Rai, and J. I. Siepmann, *J. Phys. Chem. B* **109**, 24100 (2005), <http://pubs.acs.org/doi/pdf/10.1021/jp0549125>.
- ³¹W. D. Luedtke and U. Landman, *J. Phys. Chem. B* **102**, 6566 (1998), <http://pubs.acs.org/doi/pdf/10.1021/jp981745i>.
- ³²P. Schapotschnikow, R. Pool, and T. J. Vlugt, *Comput. Phys. Commun.* **177**, 154 (2007).
- ³³J. Hautman and M. L. Klein, *J. Chem. Phys.* **91**, 4994 (1989).
- ³⁴Y. Qi, T. Çağın, Y. Kimura, and W. A. Goddard III, *Phys. Rev. B* **59**, 3527 (1999).
- ³⁵W. L. Jorgensen, D. S. Maxwell, , and J. Tirado-Rives, *J. Am. Chem. Soc.* **118**, 11225 (1996), <http://dx.doi.org/10.1021/ja9621760>.
- ³⁶J. D. Gezelter, S. Niedhart, M. Lamichhane, T. Parsons, A. Latham, J. Michalka, S. Kuang, J. Marr, K. Stocker, C. Li, C. F. Vardeman, T. Lin, C. J. Fennell, X. Sun, K. Daily, Y. Zheng, and M. A. Meineke, “OpenMD, an Open Source Engine for Molecular Dynamics,” Available at <http://openmd.org>.

- ³⁷M. A. Meineke, C. F. Vardeman, T. Lin, C. J. Fennell, and J. D. Gezelter, *J. Comput. Chem.* **26**, 252 (2005).
- ³⁸L. Martínez, R. Andrade, E. G. Birgin, and J. M. Martínez, *J. Comput. Chem.* **30**, 2157 (2009).
- ³⁹C. F. Vardeman, K. M. Stocker, and J. D. Gezelter, *J. Chem. Theory Comput.* **7**, 834 (2011).
- ⁴⁰P. J. Steinhardt, D. R. Nelson, and M. Ronchetti, *Phys. Rev. B* **28**, 784 (1983).
- ⁴¹C. F. Vardeman and J. D. Gezelter, *J. Phys. Chem. C* **112**, 3283 (2008), <http://pubs.acs.org/doi/pdf/10.1021/jp710063g>.
- ⁴²D. Segal, A. Nitzan, and P. Hänggi, *J. Chem. Phys.* **119**, 6840 (2003).
- ⁴³E. T. Swartz and R. O. Pohl, *Rev. Mod. Phys.* **61**, 605 (1989).
- ⁴⁴D. A. Young and H. J. Maris, *Phys. Rev. B* **40**, 3685 (1989).
- ⁴⁵P. Reddy, K. Castelino, and A. Majumdar, *Appl. Phys. Lett.* **87**, 211908 (2005).
- ⁴⁶A. J. Schmidt, K. C. Collins, A. J. Minnich, and G. Chen, *J. Appl. Phys.* **107**, 104907 (2010).
- ⁴⁷S. Shin, M. Kaviani, T. Desai, and R. Bonner, *Phys. Rev. B* **82**, 081302 (2010).

Supplemental Material for: Interfacial Thermal Conductance of Thiolate-Protected Gold Nanospheres

Kelsey M. Stocker, Suzanne M. Neidhart, and J. Daniel Gezelter^{a)}

*Department of Chemistry and Biochemistry, University of Notre Dame, Notre Dame,
IN 46556*

(Dated: September 24, 2018)

This document supplies force field parameters for the united-atom sites, bond, bend, and torsion parameters, as well as the cross interactions between the united-atom sites and the gold atoms. These parameters were used in the simulations presented in the main text.

^{a)}Electronic mail: gezelter@nd.edu

Gold – gold interactions were described by the quantum Sutton-Chen (QSC) model.¹ The hexane solvent is described by the TraPPE united atom model,² where sites are located at the carbon centers for alkyl groups. Bonding interactions were used for intra-molecular sites closer than 3 bonds. Effective Lennard-Jones potentials were used for non-bonded interactions.

Table I. Non-bonded interaction parameters (including cross interactions with Au atoms).

Site	mass (amu)	σ_{ii} (Å)	ϵ_{ii} (kcal/mol)	$\sigma_{\text{Au}-i}$ (Å)	$\epsilon_{\text{Au}-i}$ (kcal/mol)	source
CH ₃	15.04	3.75	0.1947	3.54	0.2146	Refs. 2, 3 and 4
CH ₂	14.03	3.95	0.09141	3.54	0.1749	Refs. 2, 3 and 4
CHene	13.02	3.73	0.09340	3.4625	0.1680	Refs. 5, 3 and 4
S	32.0655	4.45	0.2504	2.40	8.465	Refs. 4 (σ) and 3 (ϵ)
CHar	13.02	3.695	0.1004	3.4625	0.1680	Refs. 5 and 3
CH ₂ ar	14.03	3.695	0.1004	3.4625	0.1680	Refs. 5 and 3

The TraPPE-UA force field includes parameters for thiol molecules⁶ which were used for the alkanethiolate molecules in our simulations. To derive suitable parameters for butanethiolate adsorbed on Au(111) surfaces, we adopted the S parameters from Luedtke and Landman⁴ and modified the parameters for the CTS atom to maintain charge neutrality in the molecule.

Bonds are typically rigid in TraPPE-UA, so although we used equilibrium bond distances from TraPPE-UA, for flexible bonds, we adapted bond stretching spring constants from the OPLS-AA force field.⁷

To describe the interactions between metal (Au) and non-metal atoms, potential energy terms were adapted from an adsorption study of alkyl thiols on gold surfaces by Vlugt, *et al.*³ They fit an effective pair-wise Lennard-Jones form of potential parameters for the interaction between Au and pseudo-atoms CH_x and S based on a well-established and widely-used effective potential of Hautman and Klein for the Au(111) surface.⁸

Parameters not found in the TraPPE-UA force field for the intramolecular interactions of the conjugated and the penultimate alkenethiolate ligands were calculated using constrained geometry scans using the B3LYP functional^{9,10} and the 6-31G(d,p) basis set. Structures were scanned starting at the minimum energy gas phase structure for small (C₄) ligands. Only one degree of freedom was constrained for any given scan – all other atoms were allowed to minimize subject

Table II. Bond parameters.

i	j	r_0 (Å)	k_{bond} (kcal/mole/Å ²)	source
CH ₃	CH ₃	1.540	536	Refs. 2 and 7
CH ₃	CH ₂	1.540	536	Refs. 2 and 7
CH ₂	CH ₂	1.540	536	Refs. 2 and 7
CHene	CHene	1.330	1098	Refs. 5 and 7
CH ₃	CHene	1.540	634	Refs. 5 and 7
CH ₂	CHene	1.540	634	Refs. 5 and 7
S	CH ₂	1.820	444	Refs. 6 and 7
CHar	CHar	1.40	938	Refs. 5 and 7
CHar	CH ₂	1.540	536	Refs. 5 and 7
CHar	CH ₃	1.540	536	Refs. 5 and 7
CH ₂ ar	CHar	1.40	938	Refs. 5 and 7
S	CHar	1.80384	527.951	This Work

to that constraint. The resulting potential energy surfaces were fit to a harmonic potential for the bond stretching,

$$V_{\text{bond}} = \frac{k_{\text{bond}}}{2} (r - r_0)^2, \quad (1)$$

and angle bending potentials,

$$V_{\text{bend}} = \frac{k_{\text{bend}}}{2} (\theta - \theta_0)^2. \quad (2)$$

Torsional potentials were fit to the TraPPE torsional function,

$$V_{\text{tor}} = c_0 + c_1 (1 + \cos \phi) + c_2 (1 - \cos 2\phi) + c_3 (1 + \cos 3\phi). \quad (3)$$

For the penultimate thiolate ligands, the model molecule used was 2-Butene-1-thiol, for which one bend angle (S–CH₂–CHene) was scanned to fit an equilibrium angle and force constant, as well as one torsion (S–CH₂–CHene–CHene). The parameters for these two potentials also served as model for the longer conjugated thiolate ligands which require bend angle parameters for (S–CH₂–CHar) and torsion parameters for (S–CH₂–CHar–CHar).

For the C_4 conjugated thiolate ligands, the model molecule for the quantum mechanical calculations was 1,3-Butadiene-1-thiol. This ligand required fitting one bond (S–CHar), and one bend

angle (S–CHar–CHar).

The geometries of the model molecules were optimized prior to performing the constrained angle scans, and the fit values for the bond, bend, and torsional parameters were in relatively good agreement with similar parameters already present in TraPPE.

Table III. Bend angle parameters. The central atom in the bend is atom j .

i	j	k	θ_0 ($^\circ$)	k_{bend} (kcal/mol/rad 2)	source
CH ₂	CH ₂	S	114.0	124.20	Ref. 6
CH ₃	CH ₂	CH ₂	114.0	124.20	Ref. 6
CH ₂	CH ₂	CH ₂	114.0	124.20	Ref. 6
CHene	CHene	CH ₃	119.7	139.94	Ref. 5
CHene	CHene	CH ₂	119.7	139.94	Ref. 5
CH ₂	CH ₂	CHene	114.0	124.20	Ref. 5
CHar	CHar	CHar	120.0	126.0	Refs. 5 and 7
CHar	CHar	CH ₂	120.0	140.0	Refs. 5 and 7
CHar	CHar	CH ₃	120.0	140.0	Refs. 5 and 7
CHar	CHar	CH ₂ ar	120.0	126.0	Refs. 5 and 7
S	CH ₂	CHene	109.97	127.37	This work
S	CH ₂	CHar	109.97	127.37	This work
S	CHar	CHar	123.911	138.093	This work

Table IV. Torsion parameters. The central atoms for each torsion are atoms j and k , and wildcard atom types are denoted by “X”. All c_n parameters have units of kcal/mol. The torsions around carbon-carbon double bonds are harmonic and assume a trans (180°) geometry. The force constant for this torsion is given in kcal mol⁻¹degrees⁻².

i	j	k	l	c_0	c_1	c_2	c_3	source
CH ₃	CH ₂	CH ₂	CH ₂	0.0	0.7055	-0.13551	1.5725	Ref. 2
CH ₂	CH ₂	CH ₂	CH ₂	0.0	0.7055	-0.13551	1.5725	Ref. 2
CH ₂	CH ₂	CH ₂	S	0.0	0.7055	-0.13551	1.5725	Ref. 6
X	CHene	CHene	X	$V = \frac{0.008112}{2}(\phi - 180.0)^2$				Ref. 5
X	CHar	CHar	X					
CH ₂	CH ₂	CHene	CHene	1.368	0.1716	-0.2181	-0.56081	Ref. 5
CH ₂	CH ₂	CH ₂	CHene	0.0	0.7055	-0.13551	1.5725	Ref. 5
CHene	CHene	CH ₂	S	3.20753	0.207417	-0.912929	-0.958538	This work
CHar	CHar	CH ₂	S	3.20753	0.207417	-0.912929	-0.958538	This work

REFERENCES

- ¹Y. Qi, T. Çağın, Y. Kimura, and W. A. Goddard III, *Phys. Rev. B* **59**, 3527 (1999).
- ²M. G. Martin and J. I. Siepmann, *J. Phys. Chem. B* **102**, 2569 (1998).
- ³P. Schapotschnikow, R. Pool, and T. J. Vlugt, *Comput. Phys. Commun.* **177**, 154 (2007).
- ⁴W. D. Luedtke and U. Landman, *J. Phys. Chem. B* **102**, 6566 (1998), <http://pubs.acs.org/doi/pdf/10.1021/jp981745i>.
- ⁵C. D. Wick, M. G. Martin, and J. I. Siepmann, *J. Phys. Chem. B* **104**, 8008 (2000), <http://pubs.acs.org/doi/pdf/10.1021/jp001044x>.
- ⁶N. Lubna, G. Kamath, J. J. Potoff, N. Rai, and J. I. Siepmann, *J. Phys. Chem. B* **109**, 24100 (2005), <http://pubs.acs.org/doi/pdf/10.1021/jp0549125>.
- ⁷W. L. Jorgensen, D. S. Maxwell, , and J. Tirado-Rives, *J. Am. Chem. Soc.* **118**, 11225 (1996), <http://dx.doi.org/10.1021/ja9621760>.
- ⁸J. Hautman and M. L. Klein, *J. Chem. Phys.* **91**, 4994 (1989).
- ⁹A. D. Becke, *J. Chem. Phys.* **98**, 5648 (1993).
- ¹⁰C. Lee, W. Yang, and R. G. Parr, *Phys. Rev. B* **37**, 785 (1988).